Computer Physics Communications 246 (2020) 106854

Contents lists available at ScienceDirect

Computer Physics Communications

journal homepage: www.elsevier.com/locate/cpc

AhKin: A modular and efficient code for the Doppler shift attenuation method☆

Alejandro Garzón [a,*], Wilmar Rodriguez [b], Fernando Cristancho [b], Molei Tao [c]

[a] Department of Mathematics, Universidad Sergio Arboleda, Colombia
[b] Department of Physics, Universidad Nacional de Colombia, Colombia
[c] School of Mathematics, Georgia Institute of Technology, United States of America

ARTICLE INFO

Article history:
Received 6 March 2019
Received in revised form 27 June 2019
Accepted 31 July 2019
Available online 7 August 2019

Keywords:
Doppler shift attenuation method
Lifetime measurement
Gamma-ray spectroscopy
Nuclear physics
Probabilistic model

ABSTRACT

We present a set of programs for measuring lifetimes τ of nuclear states by the Doppler shift attenuation method (DSAM). The algorithms are based on the analysis of a probabilistic model of the processes occurring during a DSAM experiment. This analysis allows us to formulate the calculation of the theoretical lineshape as the application of an integral transform that converts the probability density of the cascade time (the time elapsed from nucleus creation to state decay) into the probability density of the (scaled) photon energy in the laboratory reference frame. The kernel of this integral transform, which encapsulates information related to the processes of nuclei stopping and photon detection, is independent of the state decay process, and hence needs not be recalculated on every trial of a candidate τ-value, allowing for fast computation of theoretical lineshapes. Further efficiency is gained by using algorithms that approximate continuous random variables by suitably chosen discrete ones. These codes were used to measure the lifetimes and sidefeeding times of the excited states of the normally deformed bands of ^{83}Y (Rodriguez, et al. 2019) finding for all states good agreement between the experimental lineshape and the best-fitting theoretical one.

Program summary

Program Title: AhKin
Program Files doi: http://dx.doi.org/10.17632/559kb329p2.1
Licensing provisions: MIT
Programming language: C++
Nature of problem: Measurement of lifetimes of excited nuclear states by the Doppler shift attenuation method. This involves simulating the measured energy spectrum (lineshape) of photons emitted in transitions between excited states of a nucleus traveling in a stopping material. The reduction in time of the nucleus velocity relates the state lifetime to the observed Doppler shift of the photon's energy. The measured lifetime is assumed as the value producing the theoretical lineshape that best approximates the experimental spectrum.
Solution method: A probabilistic model allows to formulate the computation of theoretical lineshapes as the evaluation of an integral transform that converts the probability density of cascade times to the Doppler-shifted photon energy spectrum. The kernel of this integral transform is independent of the state decay process, and need not be recalculated for every trial of a candidate lifetime value, permitting swift computation of lineshapes. Additional algorithmic efficiency is obtained by approximating continuous random variables by discrete ones.

1. Introduction

Measured lifetimes of excited nuclear states can be used to estimate their electric quadrupole moments and hence provide contrasting information for theoretical models of the nuclear structure [1,2]. Lifetimes of picosecond order can be determined by the Doppler shift attenuation method (DSAM) [1–8].

In a DSAM experiment, a reaction produces nuclei in excited states and with a recoiling velocity. (Examples of such reactions are fusion–evaporation and Coulomb excitation reactions [9].) The nuclei then decay to lower energy states by emission of gamma rays. Due to the nuclei's velocity, the photon's energy, as measured by detectors at rest, presents a Doppler shift. In DSAM,

☆ This paper and its associated computer program are available via the Computer Physics Communication homepage on ScienceDirect (http://www.sciencedirect.com/science/journal/00104655).

* Corresponding author.
E-mail address: alejandro.garzon@correo.usa.edu.co (A. Garzón).

https://doi.org/10.1016/j.cpc.2019.07.017
0010-4655/

the nuclei slow down in a material (backing). As a result, photons emitted early on, when the nucleus speed is "high", present a higher Doppler shift compared to photons emitted later, when the nucleus has almost stopped. Consequently, if the lifetime of the decaying nuclear state is comparable to the characteristic stopping time scale, the energy spectrum of the transition photons (lineshape) broadens and takes a shape that depends on the lifetime.

During DSAM data analysis, a theoretical calculation of the lineshape is performed. When possible, all of the many parameters affecting the calculation output are fixed at predetermined values, except for the proposed lifetime of the decaying state, which is varied while the theoretical lineshape is compared with the experimental spectrum. The value which produces the lineshape that bears the most resemblance (according to some quantitative comparison index) to the experimental spectrum is declared as the "experimentally measured lifetime".

Different codes have been written for DSAM. The program FITS [1,10] uses a one dimensional model of the nuclei slowing-down that relies on the electronic and nuclear components of the stopping power and includes the scattering of velocity directions at low energies by means of the Blaugrund approximation [11]. The codes LILIFIT [2,12], GAMMA [13,14], LINESHAPE [15,16], APCAD [17] and the one used in Ref. [18] perform a Monte Carlo simulation of the slowing-down of ions in the target and the backing that traces the ion's history of direction and speed. All of the above programs take into account the finite solid angle of the detectors and the feeding of the state through both known levels and sidefeeding states.

The contribution of this work is not a new physical model of the processes that intertwine in a DSAM experiment. Rather, we analyze a probabilistic model of the relationship between these processes, and arrive at a formulation of the computation of theoretical lineshapes in terms of an integral transform that converts the state population into the photon energy spectra. The kernel of this integral transform, containing information related to the nuclei slowing-down and photon detection, is independent of the state gamma decay, and, as a result, needs not be recomputed for each postulated lifetime value, permitting fast computation of theoretical lineshapes. Additional efficiency is attained by approximating continuous random variables by discrete ones.

Section 2 presents the random variables that determine the theoretical lineshape and introduces the continuous and discrete methods for lineshape calculation. In Section 3, the lifetime is related to the photon's energy Doppler shift. The calculation of the probability density of the cascade time (the time elapsed from nucleus creation to state decay) is described in Section 4. Section 5 shows the deduction of the integral transform for lineshape computation. The continuous method is explained in Sections 6 to 9, whereas the discrete method is presented in Section 10. The codes are described in Section 11 and applied to actual experimental data in Section 12. Section 13 summarizes this work and discusses possible improvements.

2. The probabilistic setup

As a result of the reaction used to study the nucleus of interest, many states are populated that decay by emission of gamma rays. However, when measuring lifetimes, attention is focused on a single state transition at a time, which we call the *transition of interest* and whose initial state is named the *state of interest*.

In this work, we take as the *test* with random outcome (the analogue of throwing a dice) the creation of a nucleus, which at some point of its history undergoes the transition of interest emitting a photon with wave vector direction inside the solid angle spanned by a specific detector. For instance, "One ^{83}Y nucleus makes a transition from the $25/2^+$ state to the $21/2^+$ state by emitting a photon which falls into detector n_d of the detector array". Experimental techniques are used to try to exclude data originated from any event which does not satisfy these conditions. The outcome of the test will consist of all the quantities that determine the shape of the transition energy spectrum. As we will discuss below, the Doppler shift depends on the nucleus velocity at the instant of emission of the photon, $\mathbf{u}$, and the photon wave vector direction $\hat{\mathbf{k}}$. The nucleus speed decreases (on average) as the time from its creation increases. Therefore, $\mathbf{u}$ will be related to the time ζ elapsed since the creation of the nucleus up to the instant of the photon emission. It is through ζ that the lifetime relates to the lineshape. To take into account the effect of the detector's finite solid angle span, it will be necessary to distinguish tests in which the photon was detected from those in which it went undetected. For that purpose, a discrete variable $\mathcal{D}$ is introduced which takes the values $\mathcal{D} = 0$ (undetected) and $\mathcal{D} = 1$ (detected). Together the random variables $\mathbf{u}$, $\hat{\mathbf{k}}$, ζ and $\mathcal{D}$ constitute the test outcome. Although these quantities are conceived of as observables, they are not actually measured in the experiment. However, they serve to build up a model with which the lifetime (of the state of interest) is related to the lineshape (of the transition of interest).

Two approaches were followed to compute the theoretical lineshapes. A lineshape is the probability density of the measured photon energy which is a function of other continuous random variables. The *discrete approach* consists of approximating any of the involved continuous random variables by discrete ones. Let Y be a generic continuous random variable with density $f_Y(y)$, where $f_Y(y) \neq 0$ only for $y_a < y < y_b$. The interval $[y_a, y_b]$ can be partitioned by a grid of N_Y evenly spaced points $y_i = y_a + i\Delta y$, $\Delta y = (y_b - y_a)/N_Y$, $i = 0, 1, \ldots, N_Y$. Then, the continuous random variable Y is approximated by a discrete one $\widetilde{Y}$ that can take as values only the midpoints of all subintervals $\bar{y}_i = (y_i + y_{i+1})/2$, $i = 0, 1, \ldots, N_Y - 1$, with probability $\mathcal{P}\{\widetilde{Y} = \bar{y}_i\} = \int_{y_i}^{y_{i+1}} f_Y(y)dy$. The lineshape is then approximated by performing operations with these random variables as described in Section 10. Although this approach seems intuitively valid, it is difficult to asses the accuracy with which the real lineshape is being estimated. A better approximation is provided by the *continuous method* where the probability density $f_Y(y)$ is numerically computed at the discrete set of points y_i and then linearly interpolated to produce a continuous approximation to the exact probability density. However, the discrete approach has advantages over the continuous one: it is more efficient, since it avoids performing integrations, and more robust as it circumvents the divergence to infinity of some probability densities in the limit $y \to 0$. Thus, we computed lineshapes by the continuous method as a way of validating the results of the discrete one, but provide for the software repository the code that implements the discrete method. The continuous method is presented in Sections 6 to 9, whereas the discrete approach is explained in Section 10.

3. Lifetime and Doppler shift

An excited state is characterized by quantum numbers associated to observables of angular momentum and parity among others. In the present context, it is convenient to label such states as $|\psi_i\rangle$, $i = 1, 2, \ldots$, where a particular value of i corresponds to a specific combination of quantum numbers. When undergoing spontaneous decay, a nucleus on an excited state $|\psi_1\rangle$ stays in that state for a time ξ_1, and then it makes a transition to a state of lower energy, $|\psi_2\rangle$. Similarly, for $|\psi_2\rangle$ excited, the nucleus stays in $|\psi_2\rangle$ for a period of duration ξ_2 which finishes with a transition to $|\psi_3\rangle$. This process takes place until the ground state is reached. Fig. 1 shows the evolution in time of the nuclear state over a

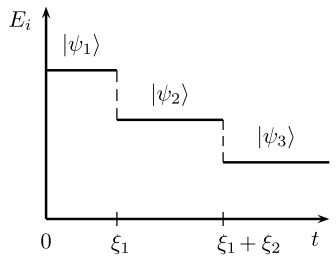

Fig. 1. Characteristic evolution of nuclear state in time. The vertical axis represents the state energy.

period on which two transitions take place. Observations over ensembles of nuclei show that the durations ξ_i are random variables whose probability density $f_{\xi_i}(t)$ are accurately approximated (for a discussion of the validity of this approximation see Ref. [19], for instance) by an exponential

$$f_{\xi_i}(t) = \frac{1}{\tau_i} e^{-t/\tau_i}, \tag{1}$$

for $t \geq 0$ and, since no realization of ξ_i is ever negative, $f_{\xi_i}(t) = 0$ for $t < 0$. The parameter τ_i is known as the mean lifetime of state $|\psi_i\rangle$ and is often called simply the lifetime. The transition from $|\psi_i\rangle$ to $|\psi_{i'}\rangle$ is signaled by the emission of a photon with energy $E_\gamma = E_i - E_{i'}$, where E_i is the energy of $|\psi_i\rangle$.

The lifetime τ_i provides information about the states $|\psi_i\rangle$ and $|\psi_{i'}\rangle$ through the relation with the transition matrix element of the interaction Hamiltonian of the electromagnetic radiation, $\mathcal{H}_{\text{int}}$ [20],

$$\frac{1}{\tau_i} \propto \langle \psi_i | \mathcal{H}_{\text{int}} | \psi_{i'} \rangle \, . \tag{2}$$

This allows to test the validity of theoretical models of the nuclear structure.

When τ_i is sufficiently small, ξ_i cannot be measured directly — Otherwise, samples of ξ_i would allow the estimation of τ_i on the basis of (1). Instead, τ_i is estimated from the probability density of a measurable quantity affected by ξ_i. For DSAM, the measurable quantity is the energy of the photon emitted in the transition $|\psi_i\rangle \to |\psi_{i'}\rangle$.

As explained above, nuclei are created with a non-zero velocity with respect to the laboratory reference frame. As a result, the energy E of photons emitted by these nuclei displays a Doppler shift when observed in this frame. The Doppler shift is determined by the velocity of the nucleus at the instant of emission $\mathbf{u}$ and the photon's wave vector direction $\hat{\mathbf{k}}$. To first order in

$$\alpha = \frac{\mathbf{u} \cdot \hat{\mathbf{k}}}{c}, \tag{3}$$

with c the speed of light, we have [21]

$$E = E_\gamma (1 + \alpha). \tag{4}$$

The nucleus velocity changes in time because it slows down inside a material. Moreover, the nucleus velocity $\mathbf{v}(t)$ measured from the instant of creation of the nucleus is a stochastic process. This is the consequence of several facts: the finite width of the distribution of projectile energies, the random linear momentum of the evaporated particles, and the random collisions the nucleus experiences while slowing down. The physics of these processes is well known, so reliable estimates of the probability density $f_{\mathbf{v}(t)}(\mathbf{r})$ are available (the model considered here is presented in Section 6). The time ζ_i (cascade time) elapsed since the creation of the nucleus until the photon emission relates $\mathbf{u}$ to $\mathbf{v}(t)$ via

$$\mathbf{u} = \mathbf{v}(\zeta_i). \tag{5}$$

ζ_i is the summation of the times spent in all the states occupied before $|\psi_i\rangle$, and therefore $\zeta_i = \xi_1 + \cdots + \xi_i$, which is also a random variable. The probability density of E, $f_E(r)$, closely related to the measured energy spectrum, is determined by the distributions of $\mathbf{v}(t)$, $\hat{\mathbf{k}}$, and ζ_i. The detector-recorded photon energy $\widetilde{E}$ is, in general, different from E, since a zero-mean random Gaussian noise δ with standard deviation σ_δ is added to E during detection, $\widetilde{E} = E + \delta$. Hence, the probability density of $\widetilde{E}$, $f_{\widetilde{E}}(r)$, is given by the convolution of $f_E(r)$ with the *detector's impulse response* $f_\delta(r)$ (the distribution of δ) [22],

$$f_{\widetilde{E}}(r) = \int_{-\infty}^{\infty} f_E(r - s) f_\delta(s) ds. \tag{6}$$

Recall that the measured energy spectrum is a histogram constructed from a sample of $f_{\widetilde{E}}(r)$. Since the value of τ_i decides the distribution of ζ_i, $f_{\zeta_i}(t)$, it also molds the measured energy spectrum. This connection is the key element of DSAM.

In what follows we calculate the distributions of $\mathbf{v}(t)$, $\hat{\mathbf{k}}$ and ζ_i and discuss how they give rise to the distribution $f_E(r)$. We begin with ζ_i.

4. The distribution of ζ_i

In this section we discuss the relation between the probability density of ζ_i, $f_{\zeta_i}(t)$, and the lifetime. In the ensuing discussion, the state of interest is labeled by the index n.

The nucleus' entry state (the state the nucleus appears on when it is created) can be any of all the states connected to the state of interest $|\psi_n\rangle$ through a sequence of physically allowed decaying transitions. Such set of states together with the particular tree topology formed by the transitions joining them is known as the *population pattern* of the state of interest. For convenience, the index i labels the states of the population pattern in such a way that if state $|\psi_{i'}\rangle$ makes a decaying transition to (populates) $|\psi_{i''}\rangle$ then $i' > i''$. It follows that the index of the state of interest n is the maximum index value and it is also the number of states of the population pattern (when including in it the state of interest itself). Fig. 3 shows a hypothetical population pattern with the corresponding state indices. The state of interest in this case is $n = 8$.

Note that with this convention the entry state is not always $|\psi_1\rangle$. Hence, it becomes more appropriate to denote by $\{i_1, i_2, \ldots, n\}$ the states visited by a cascade [For instance, $\{i_1, i_2, n\} = \{5, 7, 8\}$ for cascade (a) in Fig. 3, whereas $\{i_1, i_2, i_3, i_4, n\} = \{1, 2, 4, 6, 8\}$ for cascade (b)], in which case

$$\zeta_n = \xi_{i_1} + \xi_{i_2} + \cdots + \xi_n. \tag{7}$$

Each state in the population pattern has a probability P_i^0 of being the entry state. The probability of transitions between states is described by the *branching ratio* b_{ik}, defined as the conditional probability that state $|\psi_k\rangle$ makes a transition to $|\psi_i\rangle$, provided $|\psi_k\rangle$ has already been reached. When k is not one of the immediately preceding states of i, $b_{ik} = 0$. Moreover, $\sum_{i=1}^{n} b_{ik} = 1$, for any k. In the language of graph theory, the matrix $\mathbf{B}$ with elements b_{ik} is the generalized adjacency matrix of the edge-weighted graph associated to the population pattern. Because of the indexing convention defined above, $\mathbf{B}$ is strictly lower triangular.

When the entry state and the state of interest do not coincide, Eq. (7) can be written as

$$\zeta_n = \zeta_\nu + \xi_n, \tag{8}$$

where ζ_ν is the cascade time of the immediately preceding state $|\psi_\nu\rangle$. Due to (8) it is possible to express the probability density of ζ_n, $f_{\zeta_n}(t)$, in terms of the distributions $f_{\zeta_\nu}(t)$ of all the immediately preceding states of $|\psi_n\rangle$, each one of which, in turn, can be

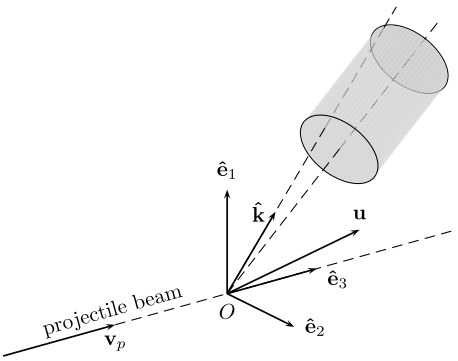

Fig. 2. Velocity of nucleus at the moment of the photon emission, $\mathbf{u}$, and photon wave vector direction, $\hat{\mathbf{k}}$, in relation to the projectile beam and the detector (cylinder). The origin O coincides with the reaction site.

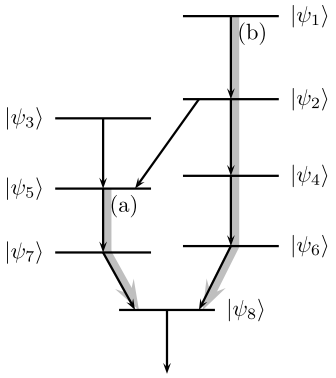

Fig. 3. Population pattern and two cascades (a) and (b) (wide gray lines).

expressed in terms of the probability densities of the cascade times of its own immediately preceding states. As proven in Appendix A, this recursive relationship, which holds for any state i, is expressed by the differential equation

$$\frac{df_{\zeta_i}}{dt} = -\lambda_i f_{\zeta_i} + \lambda_i \sum_{k=1}^{i-1} b_{ik} \frac{q_k}{q_i} f_{\zeta_k}, \tag{9}$$

where $\lambda_i = 1/\tau_i$ and q_i is the probability that the cascade of a test contains state $|\psi_i\rangle$ (particularly, $q_n = 1$), which can be computed using $q_i = P_i^0 + \sum_{k=1}^{i-1} b_{ik} q_k$. The ODE system (9) is subject to the initial condition

$$f_{\zeta_i}(0) = P_i^0/(\tau_i q_i), \tag{10}$$

as shown in Appendix A.

The relation (9) is more often found in terms of the *state populations* $P_i(t)$, defined as

$$P_i(t) = q_i \tau_i f_{\zeta_i}(t), \tag{11}$$

under the form of the *Bateman equations* [23]

$$\frac{dP_i}{dt} = -\lambda_i P_i + \sum_{k=1}^{i-1} b_{ik} \lambda_k P_k, \quad i = 1, 2, \ldots, n, \tag{12}$$

which can be obtained readily by substitution of (11) into (9).

Eqs. (9) for all the states can be gathered into a single vector equation

$$\frac{d\mathbf{f}}{dt} = A\mathbf{f}, \tag{13}$$

where $\mathbf{f} = [f_{\zeta_1}, f_{\zeta_2}, \ldots, f_{\zeta_n}]^T$ (the exponent T denotes matrix transposition) and A is a matrix with elements $a_{ii} = -\lambda_{ij}$ and $a_{ij} = \lambda_i b_{ij} q_j / q_i$. Since A is triangular, its eigenvalues are its diagonal elements $-\lambda_i$. Therefore, if no two λ_i are equal, the general solution of (13) is

$$\mathbf{f}(t) = \sum_{i=1}^{n} c_i \mathbf{d}_i e^{-\lambda_i t}. \tag{14}$$

where $\mathbf{d}_i$ is the eigenvector of A with eigenvalue $-\lambda_i$. The coefficients c_i can be found from the initial condition (10) via the linear system

$$D\mathbf{c} = \mathbf{f}_0, \tag{15}$$

where D is the lower triangular matrix with columns $\mathbf{d}_i$, $\mathbf{c} = [c_1, c_2, \ldots, c_n]^T$ and $\mathbf{f}_0 = [f_{\zeta_1}(0), f_{\zeta_2}(0), \ldots, f_{\zeta_n}(0)]^T$.

Rather than computing D and $\mathbf{c}$ each in turn, we follow a more efficient procedure to get $\mathbf{f}(t)$. The solution (14) can be written as

$$\mathbf{f}(t) = Z\boldsymbol{\eta}(t), \tag{16}$$

where $Z = D\mathbf{c}$ is a lower triangular matrix and

$$\boldsymbol{\eta}(t) = \left[e^{-\lambda_1 t}, e^{-\lambda_2 t}, \ldots, e^{-\lambda_n t}\right]^T.$$

Substitution of (16) into (15) together with use of (10) gives the following recurrence relationships for the computation of the elements z_{ij} of Z,

$$z_{ij} = \frac{1}{\lambda_i - \lambda_j} \sum_{k=j}^{i-1} a_{ik} z_{kj}, \quad j = 1, 2, \ldots, i-1, \tag{17}$$

$$z_{ii} = f_{0i} - \sum_{j=1}^{i-1} z_{ij}, \tag{18}$$

which correspond to the faster algorithm.

5. The distribution of E

In this section we derive the probability density of E from those of ζ_n, $\mathbf{v}(t)$ and $\hat{\mathbf{k}}$. In the sequel, we drop the subindex from the cascade time as we will be dealing with a single nuclear state.

Eq. (4) implies the following relationship between the probability density $f_E(r)$ and the probability density of α, $f_\alpha(r)$,

$$f_E(r) = \frac{1}{E_\gamma} f_\alpha\left(\frac{r - E_\gamma}{E_\gamma}\right). \tag{19}$$

Hence, we will focus on the calculation of $f_\alpha(r)$. For that purpose we need the probability density of $\mathbf{u}$, $f_{\mathbf{u}}(\mathbf{r})$. Assuming that $\mathbf{v}(t)$ and ζ are stochastically independent, from (5) it follows that

$$f_{\mathbf{u}|\zeta}(\mathbf{r}|t) = f_{\mathbf{v}(t)}(\mathbf{r}), \tag{20}$$

where $f_{\mathbf{u}|\zeta}(\mathbf{r}|t)$ is the conditional probability density of $\mathbf{u}$ given that $\zeta = t$. Using the law of total probabilities, we have

$$f_{\mathbf{u}}(\mathbf{r}) = \int_0^\infty f_{\mathbf{u}|\zeta}(\mathbf{r}|t) f_\zeta(t) dt \tag{21}$$

$$= \int_0^\infty f_{\mathbf{v}(t)}(\mathbf{r}) f_\zeta(t) dt. \tag{22}$$

The other piece of information required in order to calculate $f_\alpha(r)$ is the probability distribution of $\hat{\mathbf{k}}$. Only photons with direction $\hat{\mathbf{k}}$ within the solid angle spanned by the detector (as viewed from the reaction site) are susceptible of detection (see Fig. 2). Satisfaction of this condition does not grant detection, however, given the random nature of the radiation-matter interaction. As a result, the questions (i) "what is the probability that a photon that has entered the detector has done it with direction $\hat{\mathbf{k}} = \hat{\mathbf{r}}$?" (or,

more strictly speaking, with direction within a differential solid angle element around $\hat{\mathbf{r}}$) and (ii) "what is the probability that a detected photon has entered the detector with direction $\hat{\mathbf{k}} = \hat{\mathbf{r}}$?" have different answers. To distinguish the probability densities defined by the two questions we introduce the random variable $\mathcal{D}$ which takes the values $\mathcal{D} = 1$ when the photon is detected and $\mathcal{D} = 0$ when it goes undetected through the detector. Question (ii) defines the conditional probability density of $\hat{\mathbf{k}}$ given $\mathcal{D} = 1$, $f_{\hat{\mathbf{k}}|\mathcal{D}}(\hat{\mathbf{r}}|1)$. Question (i) disregards the value of $\mathcal{D}$, and hence defines the total probability density of $\hat{\mathbf{k}}$, $f_{\hat{\mathbf{k}}}(\hat{\mathbf{r}})$. Since only detected photons contribute to the energy spectrum, we must use $f_{\hat{\mathbf{k}}|\mathcal{D}}(\hat{\mathbf{r}}|1)$ in the computation of $f_\alpha(r)$. We defer to Section 7, the calculation of $f_{\hat{\mathbf{k}}|\mathcal{D}}(\hat{\mathbf{r}}|1)$ which is based on the detector geometry and $f_{\hat{\mathbf{k}}}(\hat{\mathbf{r}})$.

Eq. (3), implies

$$f_\alpha(r) = \frac{d}{dr}\int_{\mathbf{s}\cdot\hat{\mathbf{w}}/c\le r} f_{\mathbf{u}}(\mathbf{s}) f_{\hat{\mathbf{k}}|\mathcal{D}}(\hat{\mathbf{w}}|1) d^3s\, d^2w, \tag{23}$$

where we have used the stochastic independence of $\mathbf{u}$ and $\hat{\mathbf{k}}$. Substituting (23) into (22) and changing the order of integration (justified by Fubini's theorem) we have

$$f_\alpha(r) = \int_0^\infty f_{\alpha|\zeta}(r|t) f_\zeta(t) dt \tag{24}$$

where

$$f_{\alpha|\zeta}(r|t) = \frac{d}{dr}\int_{\mathbf{s}\cdot\hat{\mathbf{w}}/c\le r} f_{\mathbf{v}(t)}(\mathbf{s}) f_{\hat{\mathbf{k}}|\mathcal{D}}(\hat{\mathbf{w}}|1) d^3s\, d^2w \tag{25}$$

is the conditional probability density of α given $\zeta = t$. Eq. (24) can be seen as an integral transform, with kernel $f_{\alpha|\zeta}(r|t)$, that converts the distribution of cascade times, $f_\zeta(t)$, into the distribution of (nondimensional) shifts, $f_\alpha(r)$. In Eq. (24), the processes that determine the transition lineshape are factored into two independent expressions. On the one hand, the kernel $f_{\alpha|\zeta}(r|t)$ condenses the information pertaining to the stopping process and the detector geometry. On the other hand, the information related to the population pattern, the lifetimes, in particular, is contained in $f_\zeta(t)$. The kernel is given in the sense that it is computed on the basis of well established knowledge about the processes involved. The lifetimes are the unknown sought to be determined by the DSAM experiment. So different values of the lifetimes and different population patterns might be tried in order to fit the lineshapes while the models of the stopping process and the detector remain static. This separation into a static and a variable part of the computation of lineshapes is taken full advantage of in the formulation presented by (24). The kernel is independent of the lifetimes, so it is computed only once. The variable part, $f_\zeta(t)$ can be computed efficiently (by the method of Section 4) given that it is unconnected to the stopping and detection processes.

The code FITS uses an approximation that simplifies the calculation of the distribution of velocities, consisting of neglecting the velocity component normal to the projectile beam. Hence,

$$\mathbf{v}(t) = v_\parallel(t)\hat{\mathbf{e}}_3, \tag{26}$$

where the velocity component parallel to the beam, $v_\parallel(t)$, is a scalar stochastic process with probability density $f_{v_\parallel(t)}(r)$ and $\hat{\mathbf{e}}_3$ is a unit vector in the direction of the beam. In this case, Eq. (3) takes the form

$$\alpha = \beta\kappa, \tag{27}$$

where $\beta = u/c$, $\mathbf{u} = u\hat{\mathbf{e}}_3$, and

$$\kappa = \hat{\mathbf{k}}\cdot\hat{\mathbf{e}}_3 \tag{28}$$

is the cosine of the angle between the photon wave vector and the beam. Consequently, (25) becomes

$$f_{\alpha|\zeta}(r|t) = \int_0^\infty \frac{1}{|s|} f_{\beta|\zeta}\left(\frac{r}{s}\middle|\, t\right) f_{\kappa|\mathcal{D}}(s|1) ds, \tag{29}$$

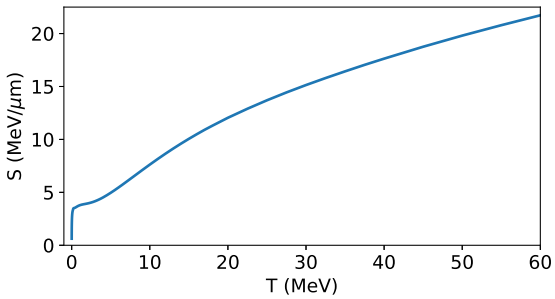

Fig. 4. Stopping power S for ^{83}Y in ^{181}Ta.

where

$$f_{\beta|\zeta}(r|t) = c f_{v_\parallel(t)}(cr) \tag{30}$$

and

$$f_{\kappa|\mathcal{D}}(r|1) = \frac{d}{dr}\int_{\hat{\mathbf{e}}_3\cdot\hat{\mathbf{s}}<r} f_{\hat{\mathbf{k}}|\mathcal{D}}(\hat{\mathbf{s}}|1) d^2s. \tag{31}$$

In the following sections we describe the computation of $f_{v_\parallel(t)}(r)$ and $f_{\kappa|\mathcal{D}}(r|1)$.

6. Slowing down of nuclei in a material

As the nucleus penetrates the stopping material, its velocity $\mathbf{v}$ changes direction with respect to the projectile beam $\hat{\mathbf{e}}_3$ by a scattering angle Θ. On average, the component of $\mathbf{v}$ normal to $\hat{\mathbf{e}}_3$ cancels out, whereas for the parallel component, the nucleus speed $v(t)$ gets multiplied by the mean of the cosine of the scattering angle $\overline{\cos\Theta}$,

$$v_\parallel(t) = v(t)\overline{\cos\Theta}.$$

Following FITS, we assume that the random initial speed $v(0)$, with distribution $f_{v(0)}(r)$, is evolved deterministically into the speed $v(t)$ according to the differential equation

$$\frac{dv}{dt} = -g(v), \tag{32}$$

where $g(v) \ge 0$ is defined below. We will find out the rule for computing the distribution of $v(t)$, $f_{v(t)}(r)$, on the basis of $f_{v(0)}(r)$.

When a nucleus performs an infinitesimal displacement dx within the stopping material, it changes its kinetic energy T by an amount $dT = -S(T)dx$, where $S(T) \ge 0$ is known as the *stopping power* [24]. (Fig. 4 shows the stopping power of ^{83}Y traveling inside ^{181}Ta, computed with the program SRIM-2008.04 [25].) Hence, T as a function of the distance x traveled inside the stopping material obeys the differential equation

$$\frac{dT}{dx} = -S(T). \tag{33}$$

Using the Newtonian expression for T,

$$T = \frac{1}{2}mv^2 \tag{34}$$

with m the nucleus mass and $v = dx/dt$, we can turn (33) into the evolution equation (32) with

$$g(v) = \frac{1}{m}S\left(\frac{1}{2}mv^2\right). \tag{35}$$

Eq. (32) implies that $v(0)$ is mapped into $v(t)$ by

$$v(t) = \Phi_t[v(0)], \tag{36}$$

where Φ_t is the time evolution operator of Eq. (32). As a consequence of the theorem on transformation of random variables, $f_{v(t)}(r)$ is related to $f_{v(0)}(r)$ by

$$f_{v(t)}(r) = \left|\frac{d}{dr}\Phi_{-t}(r)\right| f_{v(0)}\left[\Phi_{-t}(r)\right], \tag{37}$$

where we have used $\Phi_t^{-1}(r) = \Phi_{-t}(r)$. Separation of variables applied to (32) gives the following implicit relation for $\Phi_{-t}(r)$,

$$\int_r^{\Phi_{-t}(r)} \frac{du}{g(u)} = t. \tag{38}$$

Differentiation of (38) with respect to r produces

$$\frac{d}{dr}\Phi_{-t}(r) = \frac{g[\Phi_{-t}(r)]}{g(r)}. \tag{39}$$

Let $\mathcal{T}(r)$ denote the time necessary for the speed $v(t)$ to decrease from r to a very small reference value ϵ. According to (38),

$$\mathcal{T}(r) = \int_\epsilon^r \frac{du}{g(u)}. \tag{40}$$

From the definitions of $\Phi_t(r)$ and $\mathcal{T}(r)$, the following property holds

$$\mathcal{T}[\Phi_{-t}(r)] = \mathcal{T}(r) + t. \tag{41}$$

Let us define the function $\mathcal{F}(s)$ by means of

$$\mathcal{F}[\mathcal{T}(r)] = g(r) f_{v(0)}(r). \tag{42}$$

Substituting (39) into (37) and using (42) and (41), we obtain

$$f_{v(t)}(r) = \frac{\mathcal{F}\left[\mathcal{T}(r) + t\right]}{g(r)}, \tag{43}$$

which provides an efficient method for the calculation of $f_{v(t)}(r)$.

The distribution $f_{v(0)}$ is derived from the distribution of the initial kinetic energy $T(0)$, $f_{T(0)}(r)$, assumed as a normal distribution with standard deviation σ_T and mean $\overline{T}$, truncated to $\pm 3\sigma_T$ and renormalized, meaning that $f_{T(0)}(r) = 0$ for $r < \overline{T} - 3\sigma_T$ or $r > \overline{T} + 3\sigma_T$. From (34) and the theorem on transformation of random variables,

$$f_{v(0)}(r) = m r f_{T(0)}\left(\frac{1}{2}mr^2\right). \tag{44}$$

Hence $f_{v(0)}(r) = 0$ outside the interval $v_0^- \le r \le v_0^+$ with $v_0^\pm = \sqrt{2(\overline{T} \pm 3\sigma_T)/m}$. As a result, $f_{v(t)}(r)$ is non zero only in $v_-(t) \le r \le v_+(t)$, where

$$v_\pm(t) = \Phi_t(v_0^\pm) \tag{45}$$

$$= \mathcal{T}^{-1}\left[\mathcal{T}(v_0^\pm) - t\right]. \tag{46}$$

Since scattering is significant only at low kinetic energies, we assumed $\Theta = 0$ for T above a threshold, chosen as 5 MeV for the reason explained below. For T below the threshold, we used the formalism developed by Blaugrund [11] (explained in Appendix B) to obtain $\overline{\cos\Theta}$ as function of the speed v, $\overline{\cos\Theta} = \mathcal{C}(v)$. As a result $v_\parallel(t) = \mathcal{B}[v(t)]$ where

$$\mathcal{B}(v) = \begin{cases} v\,C(v), & T < 5 \text{ MeV}, \\ v, & \text{otherwise}. \end{cases}$$

In a preliminary stage, lineshapes were computed for ^{83}Y stopping in ^{181}Ta and different values of the threshold of T. It was found that the threshold value of 5 MeV produced the best fits to the experimental lineshape. Fig. 5 shows $\mathcal{C}(v)$ computed by the procedure in Appendix B.

The distribution $f_{v_\parallel(t)}(r)$ is calculated from $f_{v(t)}(r)$ via the rule for transformation of random variables

$$f_{v_\parallel(t)}(r) = \frac{1}{\mathcal{B}'[\mathcal{B}^{-1}(r)]} f_{v(t)}[\mathcal{B}^{-1}(r)], \tag{47}$$

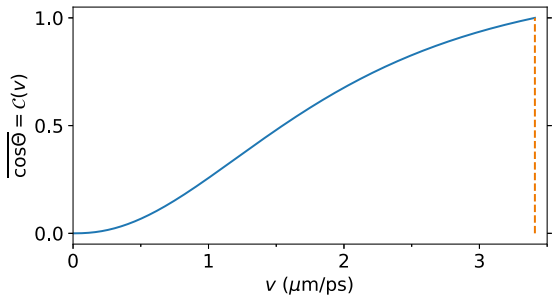

Fig. 5. Average scattering cosine as function of the speed v, $\overline{\cos\Theta} = \mathcal{C}(v)$ for ^{83}Y slowing down in ^{181}Ta. The function is defined up to $v \approx 3.41$ μm/ps (dashed line), corresponding to $T = 5$ MeV.

where the derivative of $\mathcal{B}$, $\mathcal{B}'$, is approximated by second order centered finite differences.

When $t \to \infty$, $v_\pm(t) \to 0$. In particular, $f_{v(t)}(r)$ enters the interval $[0, \epsilon]$ after the time $\mathcal{T}(v_0^-)$ and is completely inside this interval after $\mathcal{T}(v_0^+)$. Issues may arise when $v_-(t)$ approaches zero. For example, $f_{v_\parallel(t)}(\mathcal{B}[v_-(t)])$ might tend to infinity. On the other hand, we are not interested in finding the detailed shape of $f_{v_\parallel(t)}(r)$ on the interval $0 \le r < \mathcal{B}(\epsilon)$, since any variations in this narrow range will be smeared out by the multiplication of β by κ [cf. Eq. (27)] and even more so by the convolution with the detector impulse response. Thus, when $t > \mathcal{T}(v_0^-)$, we proceed as follows. For $\mathcal{B}(\epsilon) \le r \le \mathcal{B}[v_+(t)]$, we compute $f_{v_\parallel(t)}(r)$ using (47) and (43), while for $0 \le r < \mathcal{B}(\epsilon)$, we approximate $f_{v_\parallel(t)}(r)$ by a linear function ensuring continuity of $f_{v_\parallel(t)}(r)$ at $r = \mathcal{B}(\epsilon)$ and distribution normalization, $\int_0^{\mathcal{B}[v_+(t)]} f_{v_\parallel(t)}(r)dr = 1$. Moreover, it is assumed that once $f_{v_\parallel(t)}(r)$ is fully contained in the interval $[0, \mathcal{B}(\epsilon)]$, at $t = \mathcal{T}(v_0^+)$, it becomes time invariant, $f_{v_\parallel(t)}(r) = f_{v_\parallel\left[\mathcal{T}(v_0^+)\right]}(r)$ for $t > \mathcal{T}(v_0^+)$.

As an illustration, the mean kinetic energy $\overline{T}$ is computed next for a fusion–evaporation reaction. In this reaction, projectile and target nuclei fuse and produce a composite nucleus which decays by emission of nucleons and alpha particles into different *residual nuclei* (evaporation), one of which is the nucleus of interest. $\overline{T}$ is obtained on the basis of two assumptions: (i) linear momentum is conserved during the collision leading to fusion; and (ii) initially the residual nucleus moves with the speed of the composite nucleus (evaporation produces fluctuations around this speed). These lead to

$$\overline{T} = \frac{m m_p}{(m_p + m_t)^2} T_p, \tag{48}$$

where m_p and T_p are the projectile's mass and kinetic energy, respectively, and m_t is the target's mass. For example, for a collision of ^{32}S (projectile) at $T_p = 135$ MeV with ^{58}Ni (target) at rest and residual nucleus ^{83}Y, Eq. (48) gives $\overline{T} = 44.267$ MeV.

Fig. 6 shows $f_{v(t)}(r)$, computed as previously described, for ^{83}Y stopping in ^{181}Ta (cf. Fig. 4) with initial energy distribution $f_{T(0)}(r)$ given by $\overline{T} = 44.267$ MeV, as above, and $\sigma_T = 0.1\overline{T}$.

7. The distribution of wave vector directions

In this section we describe how to calculate $f_{\kappa|\mathcal{D}}(r|1)$ using (31).

We begin by computing $f_{\hat{\mathbf{k}}|\mathcal{D}}(\hat{\mathbf{r}}|1)$. A known fact [22] of the interaction of radiation with matter is that the conditional probability $\mathcal{P}\left\{\mathcal{D} = 1 \middle| \hat{\mathbf{k}} = \hat{\mathbf{r}}\right\}$ that a photon be detected given that its direction is $\hat{\mathbf{k}} = \hat{\mathbf{r}}$ is related to the length $w(\hat{\mathbf{k}})$ of the segment

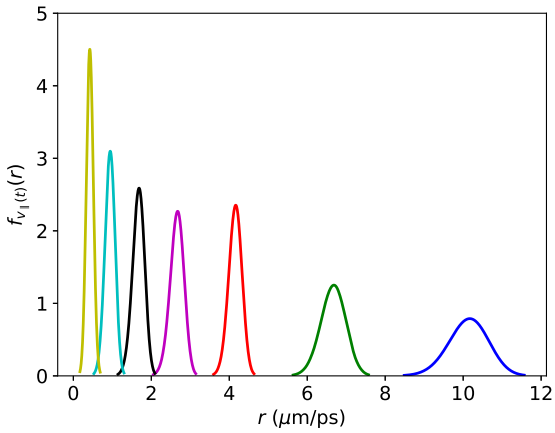

Fig. 6. Distribution $f_{v_\parallel(t)}(r)$ with r corresponding to possible values of $v_\parallel(t)$ for ^{83}Y stopping in ^{181}Ta with $\overline{T} = 44.267$ MeV and $\sigma_T = 0.1\overline{T}$, for the following times: 0 ps (blue), 0.2 ps (green), 0.45 ps (red), 0.66 ps (magenta), 0.8 ps (black), 0.92 ps (cyan) and 1.03 ps (yellow). From $t = 0.45$ ps to $t = 0.66$ ps, the distribution decreases in height due to the multiplication by the mean scattering cosine for $v < 3.41$ μm/ps . (For interpretation of the references to color in this figure legend, the reader is referred to the web version of this article.)

of the straight line along $\hat{\mathbf{k}}$ contained inside detector crystal (the *detector*, for brevity),

$$\mathcal{P}\left\{\mathcal{D}=1\,\middle|\,\hat{\mathbf{k}}=\hat{\mathbf{r}}\right\} = 1-\exp(-\mu w(\hat{\mathbf{r}})), \tag{49}$$

where μ is the crystal's coefficient of absorption. For small μw, (49) can be simplified by Taylor series expansion of its right-hand side, giving

$$\mathcal{P}\left\{\mathcal{D}=1\,\middle|\,\hat{\mathbf{k}}=\hat{\mathbf{r}}\right\} \approx \mu w(\hat{\mathbf{r}}). \tag{50}$$

Eq. (50) allows the computation of $f_{\hat{\mathbf{k}}|\mathcal{D}}(\hat{\mathbf{r}}|1)$ by means of Bayes' formula,

$$f_{\hat{\mathbf{k}}|\mathcal{D}}(\hat{\mathbf{r}}|1) = \frac{\mathcal{P}\left\{\mathcal{D}=1\,\middle|\,\hat{\mathbf{k}}=\hat{\mathbf{r}}\right\} f_{\hat{\mathbf{k}}}(\hat{\mathbf{r}})}{\mathcal{P}\{\mathcal{D}=1\}} \tag{51}$$

where

$$\mathcal{P}\{\mathcal{D}=1\} = \int_\Omega \mathcal{P}\left\{\mathcal{D}=1\,\middle|\,\hat{\mathbf{k}}=\hat{\mathbf{r}}\right\} f_{\hat{\mathbf{k}}}(\hat{\mathbf{r}}) d^2r, \tag{52}$$

is the marginal probability of a photon being detected.

In order to evaluate (31) using (51), the directions $\hat{\mathbf{r}}$ are parametrized by the two angles, θ' and ϕ', of the spherical coordinates defined with respect to a detector reference frame $\{\hat{\mathbf{e}}'_1, \hat{\mathbf{e}}'_2, \hat{\mathbf{e}}'_3\}$. The detector frame is obtained by rotation of the laboratory reference frame $\{\hat{\mathbf{e}}_1, \hat{\mathbf{e}}_2, \hat{\mathbf{e}}_3\}$ (origin O at the reaction site), with $\hat{\mathbf{e}}_3$ aligned with the projectile beam (as before), $\hat{\mathbf{e}}_1$ pointing upward, and $\hat{\mathbf{e}}_2$ completing the right-handed set (Fig. 2). In this frame, $\hat{\mathbf{r}}$ is described by the polar and azimuthal angles, θ and ϕ respectively, through the relation

$$\hat{\mathbf{r}} = \sin\theta\cos\phi\,\hat{\mathbf{e}}_1 + \sin\theta\sin\phi\,\hat{\mathbf{e}}_2 + \cos\theta\,\hat{\mathbf{e}}_3. \tag{53}$$

Let θ_d and ϕ_d denote the angular coordinates of the detector axis (which points toward the reaction site, cf. Fig. 2) in the laboratory frame. The laboratory frame is mapped into the detector frame (with $\hat{\mathbf{e}}'_i$ being the image of $\hat{\mathbf{e}}_i$) through a rotation around $\hat{\mathbf{e}}_2$ by an angle θ_d, followed by an independent rotation around $\hat{\mathbf{e}}_3$ by ϕ_d.

The expression for $w(\hat{\mathbf{r}})$ as function of the detector frame angles, $w(\theta', \phi')$, is simpler than the equivalent one for the laboratory frame angles, $w(\theta, \phi)$, hence the former is preferred. For a cylindrical detector, $w(\hat{\mathbf{r}})$ has no dependence on the azimuthal angle ϕ', $w(\hat{\mathbf{r}}) = w(\theta')$. Elementary geometry yields

$$w(\theta') = \begin{cases} H\sec\theta', & 0 \le \theta' < \theta_1, \\ R\csc\theta' - L\sec\theta', & \theta_1 \le \theta' < \theta_2, \end{cases} \tag{54}$$

where H and R are the detector's height and radius, respectively, L is the distance from the origin to the nearest detector circular face, $\tan\theta_1 = R/(L+H)$, and $\tan\theta_2 = R/L$.

The boundary of the integration region in (31), $\hat{\mathbf{e}}_3\cdot\hat{\mathbf{r}} = \text{const.}$, needs to be expressed, like the integrand, in terms of θ' and ϕ'. Let us define $h(\theta', \phi') = \hat{\mathbf{e}}_3\cdot\hat{\mathbf{r}} = \hat{\mathbf{e}}_3\cdot(\sin\theta'\cos\phi'\,\hat{\mathbf{e}}'_1 + \sin\theta'\sin\phi'\,\hat{\mathbf{e}}'_2 + \cos\theta'\,\hat{\mathbf{e}}'_3)$. Since $\hat{\mathbf{e}}_3$ is the polar axis, $h(\theta', \phi')$ is independent of the detector's azimuthal angle ϕ_d. So, without loss of generality, we can choose $\phi_d = 0$, in which case $\hat{\mathbf{e}}_3 = -\sin\theta_d\,\hat{\mathbf{e}}'_1 + \cos\theta_d\,\hat{\mathbf{e}}'_3$ and, as a result,

$$h(\theta', \phi') = -\sin\theta_d\sin\theta'\cos\phi' + \cos\theta_d\cos\theta'. \tag{55}$$

The distribution $f_{\hat{\mathbf{k}}}(\hat{\mathbf{r}})$ is the angular radiation pattern of the state transition, restricted to the solid angle spanned by the detector. Assuming the detector is narrow enough so that the radiation pattern does not change significatively within the solid angle, we approximate $f_{\hat{\mathbf{k}}}(\hat{\mathbf{r}})$ by an isotropic distribution. Let ϑ' and φ' denote the random polar and azimuthal angles of $\hat{\mathbf{k}}$ with respect to the detector frame. In terms of ϑ' and φ', $f_{\hat{\mathbf{k}}}(\hat{\mathbf{r}})$ takes the form

$$f_{\vartheta',\varphi'}(\theta', \phi') = \frac{\sin\theta'}{\Omega}, \tag{56}$$

where Ω is the solid angle of the region $0 \le \theta' \le \theta_2$ and $0 \le \phi' \le 2\pi$. Similarly, $\mathcal{P}\left\{\mathcal{D}=1\,\middle|\,\hat{\mathbf{k}}=\hat{\mathbf{r}}\right\}$ becomes

$$\mathcal{P}\left\{\mathcal{D}=1\,\middle|\,(\vartheta', \varphi') = (\theta', \phi')\right\} = \mu w(\theta'). \tag{57}$$

Substituting (56) and (57) into (51),

$$f_{\kappa|\mathcal{D}}(r|1) = \frac{1}{I(\kappa_{\max})}\frac{dI}{dr} \tag{58}$$

where

$$I(r) = \int_{h(\theta',\phi')\le r} w(\theta')\,\sin\theta' d\theta' d\phi' \tag{59}$$

and $\kappa_{\max} = \cos(\theta_d - \theta_2)$ is the maximum possible κ-value. $I(\kappa_{\min}) = 0$, where $\kappa_{\min} = \cos(\theta_d + \theta_2)$ is the minimum possible κ-value. Note that it is unnecessary to know μ since it cancels out from (58). Fig. 7 shows $f_{\kappa|\mathcal{D}}(r|1)$ obtained from numerical calculation of (59) with the function **dblquad** from the **scipy** Python module on a grid of evenly spaced points with meshsize $(\kappa_{\max} - \kappa_{\min})/100$. The derivative in (58) was approximated by the second-order centered finite-differences formula. The detector parameters are $\theta_d = 52.8°$, $R = 3.55$ cm, $H = 8$ cm, and $L = 25.5$ cm.

8. The kernel $f_{\alpha|\zeta}(r|t)$

$f_{\alpha|\zeta}(r|t)$ can now be computed evaluating the integral in (29), repeated here,

$$f_{\alpha|\zeta}(r|t) = \int_{s_{\min}}^{s_{\max}} \frac{1}{s} f_{\beta|\zeta}\left(\frac{r}{s}\,\middle|\,t\right) f_{\kappa|\mathcal{D}}(s|1) ds, \tag{60}$$

where the more precisely defined integration limits $s_{\min}$ and $s_{\max}$ are determined by the ranges over which both $f_{\beta|\zeta}(r/s|t)$ and $f_{\kappa|\mathcal{D}}(s|1)$ are different from zero: $s_{\min} = \max\{\kappa_{\min}, cr/\mathcal{B}[v^+(t)]\}$, for all times, and $s_{\max} = \min\{\kappa_{\max}, cr/\mathcal{B}[v^-(t)]\}$, when $t \le \mathcal{T}(v_0^-)$, or $s_{\max} = \kappa_{\max}$, otherwise.

Fig. 8 shows $f_{\alpha|\zeta}(r|t)$ obtained from $f_{v_\parallel(t)}(r)$ and $f_{\kappa|\mathcal{D}}(r|1)$ displayed in Figs. 6 and 7, respectively [recall that $f_{\beta|\zeta}(r|t)$ is derived from $f_{v_\parallel(t)}(r)$ using Eq. (30)]. For a given $t \le \mathcal{T}(v_0^-)$, $f_{\alpha|\zeta}(r|t)$ is non zero only in the interval $\kappa_{\min}\mathcal{B}[v_-(t)] < cr < \kappa_{\max}\mathcal{B}[v_+(t)]$.

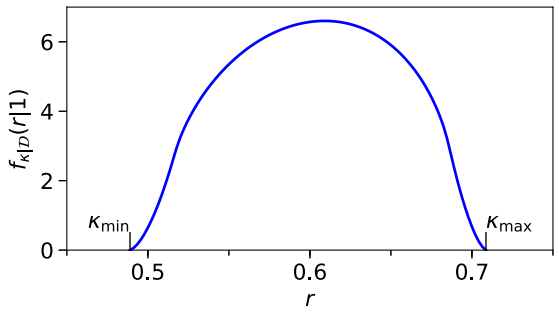

Fig. 7. Distribution $f_{\kappa|\mathcal{D}}(r|1)$ with r corresponding to possible values of κ [defined by Eq. (28)] for a cylindrical detector with parameters $\theta_d = 52.8°$, $R = 3.55$ cm, $H = 8$ cm, and $L = 25.5$ cm. The distribution is exactly zero for $r \leq \kappa_{\min}$ or $r \geq \kappa_{\max}$.

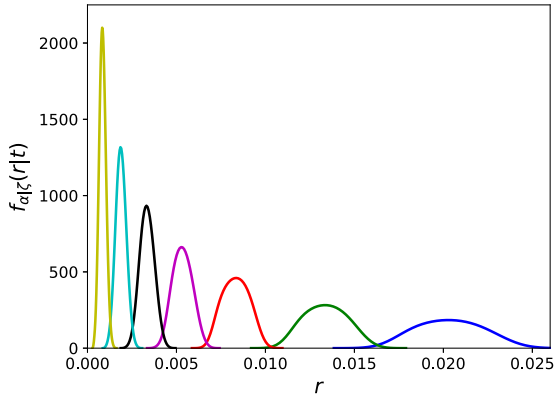

Fig. 8. The kernel $f_{\alpha|\zeta}(r|t)$ for ^{83}Y slowing down in ^{181}Ta and the detector geometry used in Fig. 7. The kernel is plotted as function of the variable r, which corresponds to possible values of α, for different times: 0 ps (blue), 0.2 ps (green), 0.45 ps (red), 0.66 ps (magenta), 0.8 ps (black), 0.92 ps (cyan) and 1.03 ps (yellow) . (For interpretation of the references to color in this figure legend, the reader is referred to the web version of this article.)

9. Computation of lineshape and measurement of the lifetime τ

The distribution $f_\alpha(r)$ is computed by Eq. (24). Let $t^\alpha_-(r)$ and $t^\alpha_+(r)$ denote the endpoints of the largest interval on which $f_{\alpha|\zeta}(r|t) > 0$, for given r. With this notation, (24) becomes

$$f_\alpha(r) = \int_{t^\alpha_-(r)}^{t^\alpha_+(r)} f_{\alpha|\zeta}(r|t) f_\zeta(t) dt \tag{61}$$

where the lower integration limit is given by

$$t^\alpha_-(r) = \begin{cases} \text{lin}(r), & 0 \leq cr < \kappa_{\min}\mathcal{B}(\epsilon) \\ t^v_-[\mathcal{B}^{-1}(cr/\kappa_{\min})], & \kappa_{\min}\mathcal{B}(\epsilon) < cr < \kappa_{\min}\mathcal{B}(v_0^-) \\ 0, & \kappa_{\min}\mathcal{B}(v_0^-) \leq cr \leq \kappa_{\max}\mathcal{B}(v_0^+) \end{cases}$$

with $\text{lin}(r) > \mathcal{T}(v_0^-)$ denoting the lower limit for the linear interpolating function and $t^v_-(r)$ defined by $v_-[t^v_-(r)] = r$, hence $t^v_-(r) = \mathcal{T}(v_0^-) - \mathcal{T}(r)$. The upper limit, on the other hand, is

$$t^\alpha_+(r) = \begin{cases} \infty, & 0 \leq cr < \kappa_{\max}\mathcal{B}(\epsilon) \\ t^v_+[\mathcal{B}^{-1}(cr/\kappa_{\min})], & \kappa_{\max}\mathcal{B}(\epsilon) \leq cr \leq \kappa_{\max}\mathcal{B}(v_0^+) \end{cases}$$

where $t^v_-(r) = \mathcal{T}(v_0^+) - \mathcal{T}(r)$. The case $t^\alpha_+(r) = \infty$ results from $f_{\alpha|\zeta}(r|t)$ becoming time invariant for $t > \mathcal{T}(v_0^+)$.

For finite $t^\alpha_+(r)$, the integral in (61) was computed by the trapezoid method using the function **trapz** from the **scipy.integrate** Python module. For $t^\alpha_+ = \infty$, the integral was split into two terms,

$$f_\alpha(r) = \int_{t^\alpha_-(r)}^{\mathcal{T}(v_0^+)} f_{\alpha|\zeta}(r|t) f_\zeta(t) dt + f_{\alpha|\zeta}[r|\mathcal{T}(v_0^+)] \int_{\mathcal{T}(v_0^+)}^{\infty} f_\zeta(t) dt, \tag{62}$$

and the first term was calculated by the trapezoid method, whereas the integral in the second one was computed analytically.

To obtain the theoretical lineshape $f_{\widetilde{E}}(r)$ using (6), $f_E(r)$ is derived from $f_\alpha(r)$ using (19), and the integral in (6), with $f_\delta(r)$ truncated to the interval $[-3.5\sigma_\delta, 3.5\sigma_\delta]$ and renormalized, is evaluated by the trapezoid method.

The dependence of the theoretical lineshape $f_{\widetilde{E}}(r)$ on the supposed value of the lifetime τ is indicated explicitly by writing it as $f_{\widetilde{E}}(r;\tau)$. To find the "real" value of τ, $f_{\widetilde{E}}(r;\tau)$ is compared with the experimental lineshape, given as a histogram of the number of photons X_i recorded with energy in any one of N_E intervals $E_i \leq E < E_{i+1}$, $i = 0, 1, \ldots, N_E - 1$, $E_i = E_0 + i\Delta E$, where ΔE is the given experimental *channel width*. The real or *measured* lifetime τ^* is assumed as the value of τ producing the theoretical lineshape that better fits the experimental one, with goodness of fit measured by the reduced chi-squared $\chi^2_r(\tau)$ [26],

$$\chi^2_r(\tau) = \frac{1}{N}\sum_{i=1}^{N} \frac{[X_i - C_Y(\tau)Y_i(\tau)]^2}{\sigma_i^2},$$

where $Y_i(\tau)$ is the probability of finding $\widetilde{E}$ in $[E_i, E_{i+1})$,

$$Y_i(\tau) = \mathcal{P}\{E_i \leq \widetilde{E} < E_{i+1}\} = \int_{E_i}^{E_{i+1}} f_{\widetilde{E}}(r;\tau) dr, \tag{63}$$

$C_Y(\tau)$ is the normalization constant

$$C_Y(\tau) = \frac{\sum_{i=1}^N X_i Y_i(\tau)}{\sum_{i=1}^N Y_i^2(\tau)},$$

and $\sigma_i = \sqrt{X_i}$, assuming the counts X_i have a Poisson distribution. More exactly, the measured τ^* is the τ-value at which $\chi^2_r(\tau)$ takes the minimum, $\chi^2_{\min}$, and the endpoints of the measurement uncertainty interval are τ_a and τ_b, $\tau_a < \tau^* < \tau_b$, such that $\chi^2_r(\tau_a) = \chi^2_r(\tau_b) = \chi^2_{\min} + 1$ [27].

10. Algorithms of the discrete method

This section explains the algorithms used by the discrete method for theoretical lineshape calculation, which approximates continuous random variables by discrete ones. In Section 12, the outcomes of this approach and the continuous method are compared.

10.1. Calculation of $f_{v_\parallel(t)}(r)$

We select a time range $[0, t_{\max}]$ and represent it with a discrete set of times $t_i = i\Delta t$, $i = 0, 1, \ldots, N_t$, $\Delta t = t_{\max}/N_t$. Similarly, we choose a velocity range $[0, v_{\max}]$, $v_0^+ < v_{\max}$, and divide it with a grid $v_i = i\Delta v$, $i = 0, 1, \ldots, N_v$, $\Delta v = v_{\max}/N_v$, where N_v is the number of grid points. The probability density $f_{v_\parallel(t_i)}(r)$, $i = 0, 1, \ldots, N_t$, is approximated by the discrete distribution $\mathcal{P}\{v_\parallel(t_i) = v_j\} = p^v_{ij}$, $j = 0, 1, \ldots, N_v - 1$, where $p^v_{ij} \approx \int_{v_j}^{v_{j+1}} f_{v_\parallel(t_i)}(r) dr$ is computed as described below.

The energy range $[\overline{T} - 3\sigma_T, \overline{T} + 3\sigma_T]$ is represented by a discrete grid $T_l = \overline{T} - 3\sigma_T + l\Delta T$, $l = 0, 1, \ldots, N_T$, $\Delta T = 6\sigma_T/N_T$, with N_T even, so that $T_{N_T/2} = \overline{T}$. The probability density $f_{T(0)}(r)$ is approximated by the discrete distribution $\mathcal{P}\{T(0) = T_l\} = p^T_l$, where $p^T_l = f_{T(0)}(T_l)/C_T$ with $C_T = \sum_{l=1}^{N_T} f_{T(0)}(T_l)$. Using this distribution, the probabilities p^v_{ij} are computed by Alg. 1.

Algorithm 1 Calculation of the discrete distribution of $v_{\|}(t)$, p_{ij}^{v}.

$s_{ij} \leftarrow 0,\ i = 0, 1, ..., N_t,\ j = 0, 1, ..., N_v - 1$
for $l \leftarrow 0, 1, ..., N_T$ **do**
  $v_l^0 \leftarrow \sqrt{2T_l/m}$
  $\widetilde{v} \leftarrow$ BuildInterpolant(v_l^0)
  for $i \leftarrow 0, 1, ..., N_t$ **do**
    $v \leftarrow \widetilde{v}(t_i)$
    $v \leftarrow \mathcal{B}(v)$
    find j such that $v \in [v_j, v_{j+1})$
    $s_{ij} \leftarrow s_{ij} + p_l^T$
  end for
end for
$p_{ij}^{v} \leftarrow s_{ij},\ i = 0, 1, ..., N_t,\ j = 0, 1, ..., N_v - 1$

In step 4 of Alg. 1, function BuildInterpolant solves Eq. (32) numerically using Runge–Kutta order four method, for initial condition v_l^0, up to $t_f > t_{\max}$, and builds a function that interpolates this solution. This interpolant is then assigned to function $\widetilde{v}$, which is called in step 6.

10.2. Calculation of $f_{\kappa|\mathcal{D}}(r|1)$

We divide the range $[-1, 1]$ with a grid of points $\kappa_i = -1 + i\Delta\kappa$, $i = 0, 1, \ldots, N_\kappa$, $\Delta\kappa = 2/N_\kappa$, and approximate the probability density $f_{\kappa|\mathcal{D}}(r|1)$ by the discrete distribution $\mathcal{P}\{\kappa = \overline{\kappa}_i\} = p_i^\kappa$, where $\overline{\kappa}_i = (\kappa_i + \kappa_{i+1})/2$, $i = 0, 1, \ldots, N_\kappa - 1$, and $p_i^\kappa \approx \int_{\kappa_i}^{\kappa_{i+1}} f_{\kappa|\mathcal{D}}(r|1)dr$ is computed by the Monte Carlo method implemented by Alg. 2.

Algorithm 2 Calculation of the discrete distribution of κ, p_i^κ

$s_i \leftarrow 0,\ i = 1, ..., N_\kappa$
for $l \leftarrow 1, 2, ..., N_{\text{shots}}$ **do**
  $y_\theta \leftarrow$ Uniform([0, 1])
  $y_\phi \leftarrow$ Uniform([0, 1])
  $\theta' \leftarrow \arccos[1 - (1 - \cos\theta_2)y_\theta]$
  $\phi' \leftarrow 2\pi y_\phi$
  $\kappa \leftarrow h(\theta', \phi')$
  find i such that $\kappa \in [\kappa_i, \kappa_{i+1})$
  $s_i \leftarrow s_i + w(\theta')$
end for
$C_\kappa \leftarrow \sum_{i=0}^{N_\kappa - 1} s_i$
$p_i^\kappa \leftarrow s_i/C_\kappa,\ i = 0, ..., N_\kappa - 1$

In step 3 of Alg. 2, Uniform([0, 1]) returns a realization of a random variable uniformly distributed on the interval [0, 1].

10.3. Calculation of $f_{\alpha|\zeta}(r|t)$

The probability density $f_{\alpha|\zeta}(r|t)$ will be approximated for the same set of times t_i, $i = 0, 1, \ldots, N_t$ as in Alg. 1. The range containing all possible α-values, $[-v_{\max}/c, v_{\max}/c]$, is divided with a grid of $2N_\alpha + 2$ points $\alpha_j = (j - 1/2)\Delta\alpha, j = -N_\alpha, \ldots - 1, 0, 1, \ldots, N_\alpha + 1$, $\Delta\alpha = 2v_{\max}/[c(2N_\alpha + 1)]$. And the probability density $f_{\alpha|\zeta}(r|t_i)$ is approximated by the discrete distribution $\mathcal{P}\{\alpha = \overline{\alpha}_j|\zeta = t_i\} = p_{ij}^{\alpha,\zeta}$, where $\overline{\alpha}_j = (\alpha_j + \alpha_{j+1})/2$ and $p_{ij}^{\alpha,\zeta} \approx \int_{\alpha_j}^{\alpha_{j+1}} f_{\alpha|\zeta}(r|t_i)dr$ is calculated by Alg. 3.

10.4. Calculation of $f_\alpha(r)$

The probability density $f_\alpha(r)$ is approximated by the discrete distribution $\mathcal{P}\{\alpha = \overline{\alpha}_j\} = p_j^\alpha \approx \int_{\alpha_{j-1}}^{\alpha_j} f_\alpha(r)dr$, where the values p_j^α

Algorithm 3 Calculation of the discrete kernel $p_{ij}^{\alpha,\zeta}$.

$s_{ij} \leftarrow 0,\ i = 0, 1, ..., N_t,\ j = 1, 2, ..., N_\alpha$
for $i \leftarrow 0, 1, ..., N_t$ **do**
  for $j \leftarrow 1, 2, ..., N_v$ **do**
    if $p_{ij}^{v} \neq 0$ **then**
      for $l \leftarrow 1, ..., N_\kappa$ **do**
        $\alpha \leftarrow v_j\overline{\kappa}_l$
        find k such that $\alpha \in [\alpha_k, \alpha_{k+1})$
        $s_{ik} \leftarrow s_{ik} + p_{ij}^{v} p_k^\kappa$
      end for
    end if
  end for
end for
$p_{ij}^{\alpha,\zeta} \leftarrow s_{ij},\ i = 0, 1, ..., N_t,\ j = -N_\alpha, ..., 0, ..., N_\alpha$

are calculated by the discrete analogue of Eq. (61),

$$p_j^\alpha = \sum_{i=i_-(j)}^{i_+(j)} p_{ij}^{\alpha,\zeta} p_i^\zeta, \tag{64}$$

where $i_-(j)$ and $i_+(j)$ are respectively the first and last indices i for which $p_{ij}^{\alpha,\zeta} \neq 0$ for a given j, and p_i^ζ are the probabilities of the discrete approximation of $f_\zeta(t)$, $\mathcal{P}\{t = t_i\} = p_i^\zeta$ where the set of t_i values is the same used by Alg. 3 and $p_i^\zeta = \int_{t_i}^{t_{i+1}} f_\zeta(t)dt$ is computed analytically.

Since $\lim_{t\to\infty} v_\pm(t) = 0$, there exists a first value i_c, such that for any $i \geq i_c$, $p_{ij}^{\alpha,\zeta} = 0$, if $j \neq 0$ and $p_{i0}^{\alpha,\zeta} = 1$. This means that $i_+(0) = \infty$ and for $j = 0$, Eq. (64) becomes

$$p_0^\alpha = p_\infty^\zeta + \sum_{i=i_-(0)}^{i_c-1} p_{ij}^{\alpha,\zeta} p_i^\zeta \tag{65}$$

where $p_\infty^\zeta = \int_{t_c}^{\infty} f_\zeta(t)dt$ with $t_c = i_c\Delta t$. Eq. (65) is analogous to (62).

10.5. Calculation of $f_E(r)$ and $f_{\overline{E}}(r)$

Let E' denote the photon energy shift, $E' = E - E_\gamma$, whose probability density $f_{E'}(r) = f_E(r - E_\gamma)$ is approximated by the discrete distribution $\mathcal{P}\{E' = \overline{E'}_i\} = p_i^{E'}$ with $\overline{E'}_i = (E'_i + E'_{i+1})/2$ and $p_i^{E'} \approx \int_{E'_i}^{E'_{i+1}} f_{E'}(r)dr$, where the grid E'_i is described next. We choose an interval $[-E'_{\max}, E'_{\max}]$ large enough as to contain the shifted interval over which the experimental lineshape is given, $[E_0 - E_\gamma, E_{N_E} - E_\gamma]$. The interval $[-E'_{\max}, E'_{\max}]$ is divided by the grid E'_i with subinterval length $\Delta E'$ ten times smaller than the experimental channel width, $E'_i = (i - 1/2)\Delta E'$, $i = -N_{E'}, \ldots, -1, 0, 1, \ldots, N_{E'} + 1$, $\Delta E' = \Delta E/10$. This grid is "congruent" with the experimental grid E_i, meaning that there exists i^* such that $E'_{i^*+10i} = E_i$. The probabilities $p_i^{E'}$ are obtained via Alg. 4

Algorithm 4 Calculation of the discrete distribution of the photon energy shift, $p_i^{E'}$

$s_i \leftarrow 0,\ i = -N_{E'}, ..., -1, 0, 1, ..., N_{E'}$
for $j \leftarrow -N_\alpha, ..., -1, 0, 1, ..., N_\alpha$ **do**
  $E' \leftarrow E_\gamma\overline{\alpha}_j$
  find i such that $E' \in [E'_i, E'_{i+1})$
  $s_i \leftarrow s_i + p_j^\alpha$
end for
$p_i^{E'} \leftarrow s_i,\ i = -N_{E'}, ..., -1, 0, 1, ..., N_{E'}$

The theoretical lineshape $f_{\widetilde{E}}(r)$ is approximated by the distribution $\mathcal{P}\{\widetilde{E} = E_\gamma + \overline{E'}_i\} = p_i^{\widetilde{E}}$, $p_i^{\widetilde{E}} \approx \int_{E'_i}^{E'_{i+1}} f_{\widetilde{E}}(E_\gamma + r)dr$, for the same grid $\overline{E'}_i$ used in Alg. 4. To approximate the convolution in (6), we use the discrete version of the detector impulse response $f_\delta(r)$, given by $\mathcal{P}\{\delta = \overline{E'}_i\} = p_i^\delta$, where $p_i^\delta = f_\delta\left(\overline{E'}_i\right)/C_\delta$ if $|\overline{E'}_i| \leq 3.5\sigma_\delta$ or $p_i^\delta = 0$ otherwise, and $C_\delta = \sum_i f_\delta(\overline{E'}_i)$. The probabilities $p_i^{\widetilde{E}}$ are obtained via the discrete analogue of the convolution in (6),

$$p_i^{\widetilde{E}} = \sum_j p_{i-j}^{E'} p_j^\delta,$$

with null terms excluded from the summation, for efficiency.

To calculate the reduced chi-squared $\chi_r^2(\tau)$, the probability $Y_i(\tau)$ defined by (63) is computed as

$$Y_i(\tau) = \sum_{j=0}^{9} P_{i^*+10i+j}^{\widetilde{E}}.$$

11. Programs

The following are the programs submitted with this work. They implement the discrete method for the calculation of the theoretical lineshape and the measurement of the lifetime. Their operation is described in the programs' documentation.

prob_cos: Computes the numerical approximation to $f_{\kappa|\mathcal{D}}(r|1)$ using Alg. 2.

stopping: Calculates the numerical approximation to the kernel $f_{\alpha|\zeta}(r|t)$ using algorithms 1 and 3.

AhKin_A: Computes $\chi_r^2(\tau)$ for a list of τ-values. Points can be added to this list interactively to refine the location of the global minimum of $\chi_r^2(\tau)$. The theoretical lineshape and $\chi_r^2(\tau)$ are calculated using the algorithms described in Sections 10.4 and 10.5.

AhKin_B: Finds a local minimum of $\chi_r^2(\tau)$ using golden section search [28]. It also determines the endpoints τ of the uncertainty interval by solving the equation $\chi_r^2(\tau) - (\chi_{\min}^2 + 1) = 0$ using the bisection method. An option allows the search range to be set so that the minimum found corresponds to the global minimum. Like **AhKin_A**, this program uses the algorithms in Sections 10.4 and 10.5 to compute the theoretical lineshape and $\chi_r^2(\tau)$.

12. A study case

The programs of the previous section were used to measure level lifetimes and sidefeeding times of the excited states of ^{83}Y populated by the fusion–evaporation reaction ^{58}Ni(^{32}S, α3p)^{83}Y at 135 MeV [29], conducted at Lawrence Berkeley National Laboratory. Evaporated particles were identified by the MICROBALL array [30], whereas gamma-rays were recorded by the GAMMASPHERE array [31], consisting of 110 HPGe detectors organized in a spherical arrangement composed by 17 rings of detectors with each ring located at a fixed polar angle θ. To select gamma-rays originated by ^{83}Y events, coincidence with the detection of one α particle and three protons was demanded. Experimental lineshapes were collected from energies recorded at four pairs of adjacent rings and, for lineshape fitting, each pair was represented by the weighted average $\bar{\theta}$ of the polar angle, yielding angles $\bar{\theta} = 35.0°, 52.8°, 127.2°$, and $145.5°$. More details of the data analysis and the measured lifetimes can be found in Ref. [29].

For all transitions analyzed, good agreement was found between the experimental lineshape and the best-fitting theoretical one. As an illustration, Fig. 9 shows the best fit to the lineshape of the transition between the $I^\pi = 45/2^-$ and $41/2^-$ states (π is parity and I is spin) of the negative parity and positive signature band, $(-,+)$, of ^{83}Y [2], with $E_\gamma = 1594.6$ keV, for all four angles. The $\chi_r^2(\tau)$ found by **AhKin_A**/**B** and the measured values τ^* of the $45/2^-$ state are displayed by Fig. 10. Fig. 11 depicts the best fit to the lineshape of a different transition, $29/2^+ \rightarrow 25/2^+$ of the $(+,+)$ band, with $E_\gamma = 1193.1$ keV. For this transition, the $\chi_r^2(\tau)$ found both by **AhKin_A**/**B** and by the continuous method are displayed by Fig. 12. Note that for all angles, **AhKin_A**/**B** and the continuous method produce the same argument minima τ^* of $\chi_r^2(\tau)$ and the same uncertainty interval $[\tau_a, \tau_b]$, $\chi_r^2(\tau_{a,b}) = \chi_{\min}^2 + 1$, thus giving identical measurements of the lifetime of the $29/2^+$ state. Moreover, at the resolution used in Fig. 11, the best fitting lineshapes generated by **AhKin_A**/**B** and the continuous method are almost indistinguishable (for this reason the latter were not plotted). This indicates that the discrete method used by **AhKin_A**/**B** provides an accurate solution of the probabilistic model for lineshape computation.

13. Concluding remarks

We presented a set of programs for measuring lifetimes of nuclear states by the Doppler shift attenuation method (DSAM). The programs compute theoretical lineshapes for proposed lifetime values τ until the value τ^* that produces the best fit to the experimental lineshape is found. Here fitness is measured by the reduced chi-squared $\chi_r^2(\tau)$. The algorithms implemented by the codes are based on a probabilistic model of the processes occurring during a DSAM experiment. The analysis of this model allows us to formulate the calculation of the theoretical lineshape as the application of an integral transform. This transform converts the probability density of the cascade time (time elapsed since the nucleus is created until it leaves the state of interest) $f_\zeta(t;\tau)$ into the probability density of the (scaled) photon energy in the laboratory reference frame (the theoretical lineshape before convolution with the detector impulse response),

$$f_\alpha(r;\tau) = \int_0^\infty f_{\alpha|\zeta}(r|t) f_\zeta(t;\tau)dt.$$

The kernel of this integral transform $f_{\alpha|\zeta}(r|t)$ contains the information related to the nucleus stopping process and the detector geometry and is independent of the cascade time. Thus, the integral transform separates the calculation of the theoretical lineshape into a static part, the kernel $f_{\alpha|\zeta}(r|t)$, that does not need to be recomputed every time a new lifetime value is tried, and a variable part, the cascade time distribution, which can be calculated efficiently since it is independent of the stopping process. This separation permits fast computation of theoretical lineshapes and, therefore, swift sampling of the curve of $\chi_r^2(\tau)$ and identification of the minimum $\chi_r^2(\tau^*)$.

The practical calculation of the lineshapes was carried out in two ways. In the continuous method, the probability densities of continuous random variables were approximated numerically at a discrete set of points, which were then linearly interpolated. In the discrete method, continuous random variables were approximated by discrete ones. The continuous method provides a theoretical lineshape which is a reliable approximation to the exact solution of the probabilistic model, the "true" lineshape, and was used to validate the discrete method. In several test cases, we found that the continuous and discrete methods produce outcomes that for practical purposes are identical. Here, we present programs implementing the algorithms of the discrete method since they are much faster than those of the continuous one.

The following are the codes attached to this work. Program **stopping** computes the kernel using a one-dimensional model of the stopping process that includes a scattering angle at low kinetic energies. It takes as input the distribution of the projection of the photon direction onto the projectile beam, calculated by program **prob_cos**, which takes into account the detector's

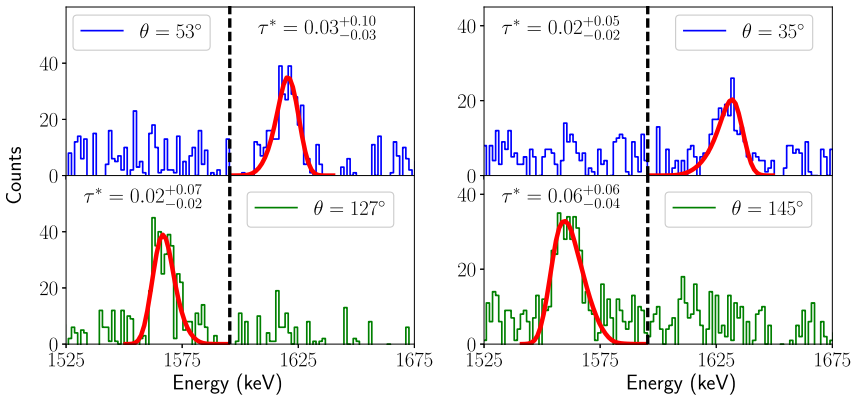

Fig. 9. Best fit (smooth solid line) to the experimental lineshape (histogram) of the $45/2^- \rightarrow 41/2^-$ transition of the $(-,+)$ band, with $E_\gamma = 1594.6$ keV, found by **AhKin_B** for four different detector polar angles. For each angle, the (rounded) measured lifetime of state $45/2^-$ is displayed.

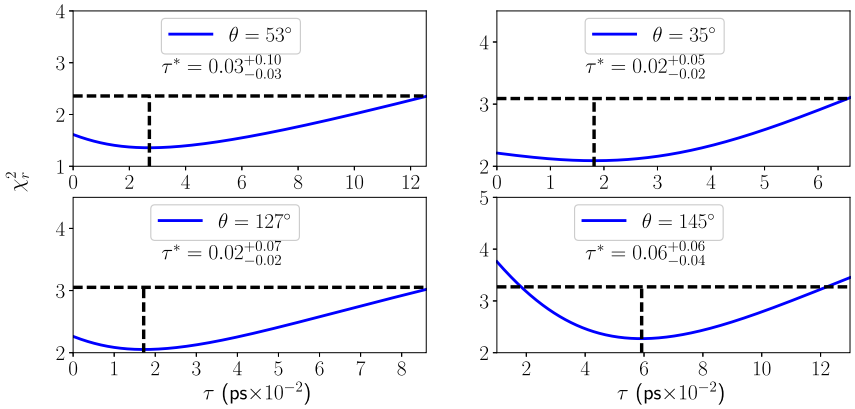

Fig. 10. $\chi^2_r(\tau)$ of the fit to the experimental lineshape of the $45/2^- \rightarrow 41/2^-$ transition of the $(-,+)$ band, found by **AhKin_A**/**B**. On each subplot, the vertical dashed line marks the argument minimum τ^* of $\chi^2_r(\tau)$, $\chi^2_r(\tau^*) = \chi^2_{\text{min}}$, while the horizontal dashed line indicates $\chi^2_{\text{min}} + 1$.

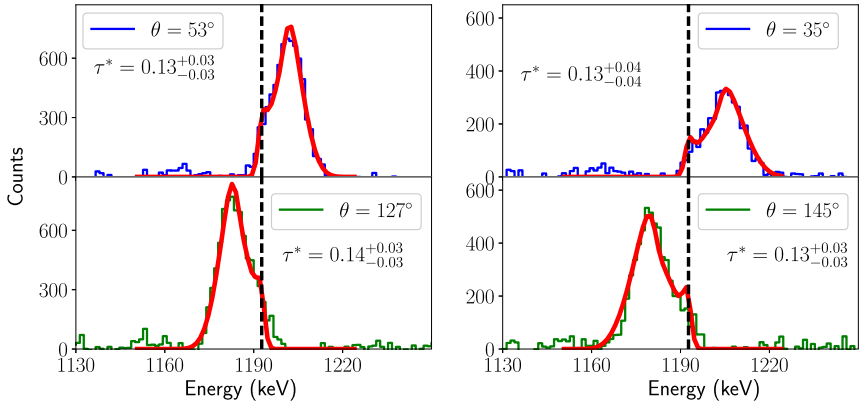

Fig. 11. Best fit (smooth solid line) to the experimental lineshape (histogram) of the $29/2^+ \rightarrow 25/2^+$ transition of the $(+,+)$ band, with $E_\gamma = 1193.1$ keV, found by **AhKin_B** for four different detector polar angles. For each angle, the (rounded) measured lifetime of state $29/2^+$ is displayed.

angular aperture. Program **AhKin_A** takes the kernel as input and computes the theoretical lineshape (performing the integral transform) and $\chi^2_r(\tau)$ for a list of τ-values that can be easily refined interactively. It can be used to obtain an estimate of the global minimum of $\chi^2_r(\tau)$. **AhKin_B** finds automatically the global minimum of $\chi^2_r(\tau)$ (if the search range is suitably set) and the limits of the uncertainty interval, hence providing the measurement of τ.

This set of programs has been used to measure the lifetimes of states of ^{83}Y populated by the fusion–evaporation reaction ^{58}Ni($text^{32}$S, α3p)^{83}Y at 135 MeV, conducted at Lawrence Berkeley National Laboratory, with evaporated charged particles and gamma-rays detected by the MICROBALL and GAMMASPHERE arrays, respectively [29]. In most cases, we found good agreement between the experimental lineshapes and the best-fitting theoretical one, which gives us confidence that the physical model used and the solution implemented in the code are reliable.

As future work, calculation of the kernel using a more accurate model of the interaction of nuclei with matter could be pursued. The new model might consider the angular dispersion

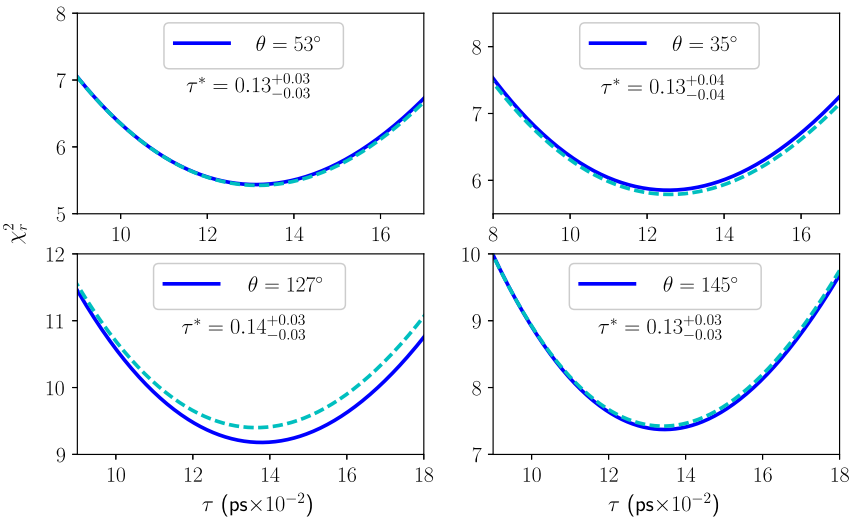

Fig. 12. $\chi^2_r(\tau)$ of the fit to the experimental lineshape of the $29/2^+ \rightarrow 25/2^+$ transition of the $(+,+)$ band, found by **AhKin_A**/**B** (solid blue line) and by the continuous method (dashed cyan line) for four different detector polar angles. (For interpretation of the references to color in this figure legend, the reader is referred to the web version of this article.)

of the residual nuclei's initial velocity, estimated theoretically or experimentally from the energies of the evaporated particles, and the finite width of the target film. It might also simulate three dimensional collisions of the residual nuclei with atoms of the backing [32]. This new kernel could be used by the current versions of programs **AhKin_A** and **AhKin_B**, i.e. without any need for source code changes, due to the separation of kernel and lineshape computation. Hence, this modularity not only contributes to the code's efficiency but also facilitates updating the simulation model.

Declaration of competing interest

The authors declare that they have no known competing financial interests or personal relationships that could have appeared to influence the work reported in this paper.

Acknowledgments

WR acknowledges partial support from Colciencias, contract Nr. 617 "Becas doctorados nacionales". MT acknowledges partial support by National Science Foundation grants DMS-1521667, ECCS-1829821 and DMS-1847802.

Appendix A. Recurrence formula for probability densities $f_{\zeta_i}(t)$

The index ν of the immediately preceding state of $|\phi_n\rangle$ is a random variable that takes values in the set U_n of all possible immediately preceding states (for $n = 8$ in Fig. 3, $U_8 = \{6, 7\}$). We extend the definition of ν to include the case in which $|\phi_n\rangle$ is the entry state, which is assigned the value $\nu = 0$. The different cases can be summarized as

$$\zeta_n = \begin{cases} \xi_n, & \nu = 0, \\ \zeta_\nu + \xi_n, & \nu \in U_n, \end{cases} \tag{A.1}$$

where U_n is the set of all possible immediately preceding states of $|\psi_n\rangle$. In calculating the probability density of ζ_i we take into account the contributions of all the possible cases listed by (A.1) (with n substituted by i). Using the law of total probabilities:

$$f_{\zeta_i}(t) = \frac{P_i^0}{q_i} f_{\zeta_i|\nu}(t|0) + \sum_{k\in U_i} b_{ik}\frac{q_k}{q_i} f_{\zeta_i|\nu}(t|k), \tag{A.2}$$

where $f_{\zeta_i|\nu}(t|k)$ is the conditional probability density of ζ_i given that $\nu = k$. We divided the probabilities P_i^0 and q_k by q_i in order to condition on cascades that contain $|\psi_i\rangle$. From (A.1) we see that

$$f_{\zeta_i|\nu}(t|0) = f_{\xi_i}(t) \tag{A.3}$$

and

$$f_{\zeta_i|\nu}(t|k) = f_{\zeta_k+\xi_i}(t). \tag{A.4}$$

Since the times $\xi_1, \xi_2, \ldots, \xi_i$ are independent random variables, so are ζ_k and ξ_i. Consequently,

$$f_{\zeta_k+\xi_i}(t) = \int_{-\infty}^{\infty} f_{\zeta_k}(s) f_{\xi_i}(s-t)ds. \tag{A.5}$$

Substituting (1) into (A.5), we have

$$f_{\zeta_k+\xi_i}(t) = \frac{1}{\tau_i} e^{-t/\tau_i} \int_0^t f_{\zeta_k}(s) e^{-s/\tau_i} ds. \tag{A.6}$$

Substitution of (A.3), (A.4), (1) and (A.6) into (A.2), yields

$$f_{\zeta_i}(t) = \frac{1}{\tau_i} e^{-t/\tau_i} \left(\frac{P_i^0}{q_i} + \sum_{k\in U_i} b_{ik}\frac{q_k}{q_i} \int_0^t f_{\zeta_k}(s) e^{s/\tau_i} ds \right). \tag{A.7}$$

Eq. (A.7) is the desired recurrence formula. We can formulate this recurrence formula as a differential equation taking the derivative on both sides of (A.7) to obtain

$$\frac{df_{\zeta_i}}{dt} = -\frac{f_{\zeta_i}}{\tau_i} + \frac{1}{\tau_i} \sum_{k\in U_i} b_{ik}\frac{q_k}{q_i} f_{\zeta_k}. \tag{A.8}$$

Considering that $b_{ik} = 0$ if k does not populate i, leads to (9). The required initial condition for (A.8) can be found by evaluating (A.7) at $t = 0$, which yields $f_{\zeta_i}(0) = P_i^0/(\tau_i q_i)$.

Appendix B. Computation of the average scattering angle cosine, $\overline{\cos\Theta}$

We obtain $\overline{\cos\Theta}$ as function of the kinetic energy T using the formalism developed by Blaugrund [11], whose equations are expressed in terms of a nondimensional kinetic energy ε defined by

$$\varepsilon = 10.2 \frac{\mathcal{M}}{A_1} \frac{T}{m_e c^2} \tag{B.1}$$

where m_e is the mass of the electron and

$$\mathcal{M} = \frac{1.63 \times 10^3 A_1 A_2}{Z_1 Z_2 \left(Z_1^{2/3} + Z_2^{2/3}\right)^{1/2} (A_1 + A_2)}$$

with A_i and Z_i denoting respectively the mass and atomic numbers of the residual nucleus ($i = 1$) and the stopping material ($i = 2$). For ^{83}Y stopping in ^{181}Ta, $A_1 = 83$, $Z_1 = 39$, $A_2 = 181$, and $Z_2 = 73$.

The mean scattering cosine is computed by

$$\overline{\cos\Theta} = \widetilde{\mathcal{C}}(\varepsilon) \equiv \exp\left[-\frac{1}{2}\frac{A_2}{A_1} G I(\varepsilon)\right] \tag{B.2}$$

where

$$G = \begin{cases} 1 + \frac{2}{3} r - \frac{7}{15} r^2, & r < 1 \\ \frac{2}{3} + \frac{8}{15}\frac{1}{r}, & r > 1 \end{cases}$$

with $r = A_1/A_2$, and

$$I(\varepsilon) = \int_{\varepsilon}^{\varepsilon_0} \frac{S_n(z)}{z\,[S_n(z) + S_e(z)]} dz$$

where ε_0 corresponds to the "initial" kinetic energy $T = 5$ MeV, and $S_n(\varepsilon)$ and $S_e(\varepsilon)$ are respectively the nondimensional atomic and electronic stopping power, approximated as

$$S_n(\varepsilon) = 0.6111 e^{-\sqrt{\varepsilon}/1.919}\left(1 - e^{-\sqrt{\varepsilon}/0.2406}\right)$$

and

$$S_e(\varepsilon) = k\sqrt{\varepsilon}, \tag{B.3}$$

where

$$k = Z_1^{1/6} \frac{0.0793 Z_1^{1/2} Z_2^{1/2} (A_1 + A_2)^{3/2}}{\left(Z_1^{2/3} + Z_2^{2/3}\right)^{3/4} A_1^{3/2} A_2^{1/2}}.$$

Using (B.1), (B.2), and (34), the mean scattering cosine can be expressed as a function of the speed v, $\overline{\cos\Theta} = \mathcal{C}(v)$.

References

[1] R. Cardona, F. Cristancho, S.L. Tabor, R.A. Kaye, G.Z. Solomon, J. Döring, G.D. Johns, M. Devlin, F. Lerma, D.G. Sarantites, I.-Y. Lee, A.O. Macchiavelli, I. Ragnarsson, Phys. Rev. C 68 (2003) 024303.

[2] T.D. Johnson, A. Aprahamian, C.J. Lister, D.J. Blumenthal, B. Crowell, P. Chowdhury, P. Fallon, A.O. Machiavelli, Phys. Rev. C 55 (1997) 1108.

[3] D.N. Poenaru, W. Greiner, Experimental Techniques in Nuclear Physics, Walter de Gruyter, New York, 1997.

[4] A. Ertoprak, B. Cederwall, C. Qi, M. Doncel, U. Jakobsson, B.M. Nyakó, G. Jaworski, P. Davies, G. de France, I. Kuti, D.R. Napoli, R. Wadsworth, S.S. Ghugre, R. Raut, B. Akkus, H. Al Azri, A. Algora, G. de Angelis, A. Atac, T. Bäck, A. Boso, E. Clément, D.M. Debenham, Z. Dombrádi, S. Ertürk, A. Gadea, F. Ghazi Moradi, A. Gottardo, T. Hüyük, E. Ideguchi, H. Li, C. Michelagnoli, V. Modamio, J. Nyberg, M. Palacz, C.M. Petrache, F. Recchia, M. Sandzelius, M. Siciliano, J. Timár, J.J. Valiente-Dobón, Z.G. Xiao, Eur. Phys. J. A 54 (2018) 145.

[5] S. Rajbanshi, R. Raut, H. Pai, S. Ali, A. Goswami, S. Bhattacharyya, G. Mukherjee, R.K. Bhowmik, S. Muralithar, R.P. Singh, G. Gangopadhyay, M. Kumar Raju, P. Singh, Phys. Rev. C 98 (2018) 061304(R).

[6] M. Ionescu-Bujor, S. Aydin, N. Mărginean, C. Costache, D. Bucurescu, N. Florea, T. Glodariu, A. Ionescu, A. Iordăchescu, R. Mărginean, C. Mihai, R.E. Mihai, A. Mitu, A. Negreț, C.R. Niță, A. Olăcel, S. Pascu, B. Saygi, L. Stroe, R. Suvăilă, S. Toma, A. Turturică, Phys. Rev. C 98 (2018) 054305.

[7] P. Banerjee, S. Ganguly, M.K. Pradhan, M. Moin Shaikh, H.P. Sharma, S. Chakraborty, R. Palit, R.G. Pillay, V. Nanal, S. Saha, J. Sethi, Phys. Rev. C 98 (2018) 034320.

[8] C. Mihai, A.A. Pasternak, S. Pascu, D. Filipescu, M. Ivaşcu, D. Bucurescu, G. Căta-Danil, I. Căta-Danil, D. Deleanu, D.G. Ghiță, T. Glodariu, N. Mărginean, R. Mărginean, A. Negret, T. Sava, L. Stroe, G. Suliman, N.V. Zamfir, Phys. Rev. C 83 (2011) 054310.

[9] H. Ejiri, M.J.A. de Voigt, Gamma-ray and electron Spectroscopy in Nuclear Physics, Oxford Sciences Publications, Oxford, UK, 1989.

[10] E.F. Moore, P.D. Cottle, C.J. Gross, D.M. Headly, U.J. Hüttmeier, S.L. Tabor, W. Nazarewicz, Phys. Rev. C 38 (1988) 696.

[11] A.E. Blaugrund, Nucl. Phys. 88 (1966) 501–512.

[12] H. Emling, I. Ahmad, P.J. Daly, B.K. Dichter, M. Drigert, U. Garg, Z.W. Grabowski, R. Holzmann, R.V.F. Janssens, T.L. Khoo, W.C. Ma, M. Piiparinen, M.A. Quader, I. Ragnarsson, W.H. Trzaska, Phys. Lett. B 217 (1989) 33–37.

[13] C. Mihai, A.A. Pasternak, D. Filipescu, M. Ivaşcu, D. Bucurescu, G. Căta-Danil, I. Căta-Danil, D. Deleanu, D. Ghiță, T. Glodariu, Y.N. Lobach, N. Mărginean, R. Mărginean, A. Negret, S. Pascu, T. Sava, L. Stroe, G. Suliman, N.V. Zamfir, Phys. Rev. C 81 (2010) 034314.

[14] J. Srebrny, C. Droste, T. Morek, K. Starosta, A.A. Wasilewski, A.A. Pasternak, E.O. Podsvirova, Y.N. Lobach, G.H. Hagemann, S. Juutinen, M. Piiparinen, S. Törmänen, A. Virtanen, Nuclear Phys. A 683 (2001) 21–47.

[15] N.R. Johnson, J.C. Wells, Y. Akovali, C. Baktash, R. Bengtsson, M.J. Brinkman, D.M. Cullen, C.J. Gross, H.-Q. Jin, I.-Y. Lee, A.O. Macchiavelli, F.K. McGowan, W.T. Milner, C.-H. Yu, Phys. Rev. C 55 (2) (1997) 652–659.

[16] J.C. Wells, N.R. Johnson, A computer program for doppler-broadened lineshape analysis, Tech. Rep. ORNL-6689, ORNL (1991).

[17] C. Stahl, J. Leske, M. Lettmann, N. Pietralla, Comput. Phys. Comm. 214 (2017) 174–198.

[18] P. Petkov, A. Dewald, D. Tonev, N. Goutev, G. Asova, B. Dimitrov, G. Gavrilov, M.N. Mineva, M.S. Yavahchova, Nucl. Instrum. Methods Phys. Res. A 783 (2015) 6–11.

[19] P.J. Aston, Europhys. Lett. 97 (2012) 52001.

[20] A. DeShalit, H. Feshbach, Theoretical Nuclear Physics, Volume I: Nuclear Structure, John Wiley & Sons, New York, 1974.

[21] A.P. French, Special Relativity, W.W. Norton & Company, Inc., New York, 1968.

[22] W.R. Leo, Techniques for Nuclear and Particle Physics Experiments, Springer-Verlag, Berlin, 1994.

[23] H. Bateman, Proc. Camb. Phil. Soc. Math. Phys. Sci. 15 (1910) 423–427.

[24] J.F. Ziegler, J.P. Biersack, U. Littmark, The Stopping and Range of Ions in Solids, Pergamon Press, New York, 1985.

[25] J.F. Ziegler, Interactions of Ions with Matter, [Online; accessed 01-Dec-2017] (2017). URL http://www.srim.org/.

[26] L. Lyons, Statistics for Nuclear and Particle Physicists, Cambridge University Press, Cambridge, UK, 1986.

[27] D.W.O. Rogers, Nucl. Instrum. Methods 127 (1975) 253–260.

[28] W.H. Press, S.A. Teukolsky, W.T. Vetterling, B.P. Flannery, Numerical Recipes in C, Cambridge University Press, Cambridge, UK, 1992.

[29] W. Rodriguez, F. Cristancho, S.L. Tabor, A. Kardan, I. Ragnarsson, R.A. Haring-Kaye, J. Döring, D.G. Sarantites, A. Garzón, Phys. Rev. C (2019) in press.

[30] D.G. Sarantites, P.-F. Hua, M. Devlin, L.G. Sobotka, J. Elson, J.T. Hood, D.R. LaFosse, J.E. Sarantites, M.R. Maier, Nucl. Instrum. Methods Phys. Res. A 381 (1996) 418–432.

[31] I.-Y. Lee, Nuclear Phys. A 520 (1990) c641–c655.

[32] J.F. Ziegler, M. Ziegler, J.P. Biersack, Nucl. Instrum. Methods Phys. Res. B 268 (2010) 1818–1823.